Investigating solute transport and reaction using a mechanistically coupled geochemical and geophysical modeling approach

Flore Rembert, Nicole M Fernandez, Linda Luquot, Roger Guérin, Damien Jougnot

To cite this version:

Flore Rembert, Nicole M Fernandez, Linda Luquot, Roger Guérin, Damien Jougnot. Investigating solute transport and reaction using a mechanistically coupled geochemical and geophysical modeling approach. Advances in Water Resources, 2024, 196, pp.104879. 10.1016/j.advwatres.2024.104879 . hal-04845998v1

HAL Id: hal-04845998
https://univ-orleans.hal.science/hal-04845998v1

Submitted on 18 Dec 2024 (v1), last revised 6 Jan 2025 (v2)

Graphical Abstract

Investigating solute transport and reaction using a mechanistically coupled geochemical and geophysical modeling approach

Flore Rembert, Nicole M Fernandez, Linda Luquot, Roger Guérin, Damien Jougnot

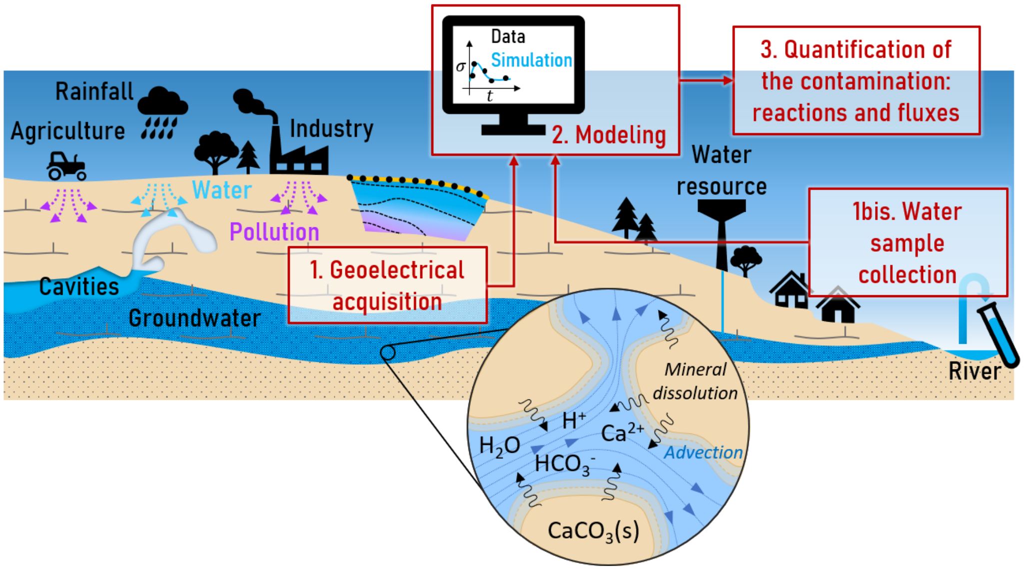

Highlights

Investigating solute transport and reaction using a mechanistically coupled geochemical and geophysical modeling approach

Flore Rembert, Nicole M Fernandez, Linda Luquot, Roger Guérin, Damien Jougnot

- Geoelectrical methods are used to quantitatively monitor reactive contamination
- Calcite dissolution under different regimes is studied as an example of reactive process
- Reactive transport simulation is coupled with petrophysical modeling
- Self-potential monitoring allows the spatialization of the reactive zone
- Electrical conductivity shows significant variations during intense dissolution regime

Investigating solute transport and reaction using a mechanistically coupled geochemical and geophysical modeling approach

Flore Rembert[a,d], Nicole M Fernandez[b], Linda Luquot[c], Roger Guérin[d], Damien Jougnot[d]

[a] *Univ. Orléans, CNRS, BRGM, ISTO, UMR 7327, Orléans, F-45071, France*
[b] *Department of Earth and Atmospheric Sciences, Cornell University, Ithaca, NY, USA*
[c] *Géosciences Montpellier, Univ Montpellier, CNRS, Univ Antilles, Montpellier, F-34095, France*
[d] *Sorbonne Université, CNRS, EPHE, METIS, Paris, F-75005, France*

Abstract

The use of geoelectrical monitoring of groundwater quality and contamination is a growing and promising topic. Nowadays, geoelectrical methods are mostly used as qualitative detection tools. This study aims to better use geoelectrical signals as a complementary tool for the quantitative characterization of chemical species transport and reaction in the porous matrix by developing a coupled mechanistic model. We examine the dissolution of calcite as an effective proof-of-concept. Our investigation focuses on the impact of the reactive zone's position, extent, and intensity of geoelectrical signals under various inlet conditions. We conducted five experiments on flow-through columns equipped with geoelectrical monitoring. This study presents a unique dataset that is analyzed using a workflow that combines reactive transport numerical simulation with numerical modeling of geoelectrical and structural properties. The comparison of the predicted signals with the experimental data clearly shows the characterization of the spatial

Preprint submitted to Advances in Water Resources *November 29, 2024*

and temporal distributions of the reaction rates.

Keywords: Calcite dissolution, Reactive transport modeling, Geophysics, Self-potential, Spectral induced polarization

---

1. Introduction

Transport, mixing, and reaction of solutes are ubiquitous issues in characterizing the fate of groundwater contaminants (e.g., Dentz et al., 2011). For example, saline intrusion in coastal aquifers and hyporheic zones within river channels are important places of active mixing and reactivity (e.g., Werner et al., 2013; Boano et al., 2014). In carbonate environments, there is a strong need for monitoring of fluid injection and associated dissolution and precipitation processes dedicated to environmental engineering. These needs for carbonate reservoirs gather applications such as precipitation-based remediation for confinement barriers and soil consolidation, carbon dioxide (CO_2) sequestration, geothermal doublet, artificial recharge, or karst aquifer remediation and phantomization (e.g., Benson et al., 2005; Kaufmann and Deceuster, 2014; Ahmad et al., 2020; Knappett et al., 2020). The common methods to quantify the flow and solute transport are water sampling and conservative tracer tests (e.g., Bufflap and Allen, 1995; Goldscheider et al., 2008). However, these methods rely on a grid of multi-level monitoring wells, from which it is often difficult to determine the flow path and the position, shape, and extent of a tracer plume (e.g., Kemna et al., 2002). In addition to the fact that these methods are intrusive, provide limited and spatially restricted information, and are generally expensive, the use of conservative tracers appears controversial because ionic exchange and rate-limited mass transfer are difficult to capture (e.g., Singha et al., 2011).

Environmental geophysics offers the possibility of extended high-resolution monitoring of the heterogeneous and dynamic subsurface with 2D and 3D surveys (even 4D considering the time) (e.g., Hermans et al., 2023). Geophysical methods measure the distribution and evolution of physical properties in geological media (e.g., electrical conductivity, magnetic susceptibility, density, seismic wave velocity). Appropriate mechanistic models allow these properties to be expressed in terms of hydrochemical parameters of interest (e.g., porosity, permeability, chemical composition, water content). Some geophysical methods are deployed to address specific hydrogeological problems (e.g., Rubin and Hubbard, 2006; Hubbard and Linde, 2011; Binley et al., 2015). This discipline is called hydrogeophysics and among the existing geophysical techniques, geoelectrical methods show strong capabilities for imaging structures and dynamic processes (e.g., Daily et al., 1992; Revil et al., 2012a; Singha et al., 2015; Kaufmann and Romanov, 2016). Enhanced sensitivity of electrical properties (electrical conductivity and dielectric permittivity) to pore water chemistry and dynamics has improved salt tracer monitoring field experiments, imaging plumes non-intrusively with an unprecedented high spatial and temporal resolution compared to traditional sample collection (e.g., Singha and Gorelick, 2005; Cassiani et al., 2006; Jougnot et al., 2015). More recently, saline intrusion has been studied with geoelectrical methods (e.g., MacAllister et al., 2018; Palacios et al., 2020). Some studies also have applied such techniques to better characterize changes in flow and transport behavior driven by living organisms and contaminants (e.g., Ghosh et al., 2018; Kessouri et al., 2019; Saneiyan et al., 2019; Flores Orozco et al., 2021).

To enhance understanding of the role played by reactive transport in groundwater flow, laboratory studies are carried out at various scales (μm to m). Column experiments are traditionally used for percolation studies (e.g., Wu et al., 2010; Singha et al., 2011; Izumoto et al., 2020; Ben Moshe and Furman, 2022). To explore heterogeneous behavior (e.g., partially saturated conditions, local mixing, complex porous rock matrix), core sample experiments with tomographic imaging (e.g., Rembert et al., 2023a) and micro–millifluidic experiments are conducted (e.g., Jougnot et al., 2018; Sun et al., 2021; Izumoto et al., 2022; Fernandez Visentini et al., 2023; Rembert et al., 2023b). However, studies addressing the electrical signature of reactive chemical transport (e.g., adsorption, mineral dissolution–precipitation) are scarce (e.g., Ben Moshe et al., 2021; Bate et al., 2021). This knowledge gap arises in part from the inherent complexity of reactions between fluids and solids within porous media, which are inherently non-conservative and, thus, distinct from simpler systems such as sodium chloride (NaCl) intrusion (e.g., Maineult et al., 2004, 2006). For example, in the study of carbonate dissolution–precipitation, the literature shows diverging electrical results. Some authors report no or minor complex electrical conductivity variations related to calcite precipitation or dissolution (e.g., Zhang et al., 2012; Halisch et al., 2018), while other studies present results strongly impacted (e.g., Saneiyan et al., 2019); highlighting the notable challenges that still exist in modeling electrical signatures of fluid-mineral interactions. In some studies, the electrochemical coupling is oversimplified considering it as an additional empirical constant (e.g., Cherubini et al., 2019), while it can henceforth be addressed when reactivity is treated with a robust method provided by reactive transport simulation (e.g., Rembert et al., 2022).

This study aims to focus on the geoelectrical signature of calcite dissolution as an example of reactive contamination of pore water since it is a ubiquitous, well-studied reaction, and highly representative of fluid-mineral reactivity. We performed five column-experiments of reactive percolation. We evaluated the impact of using weak or strong acids for the injection in promoting calcite dissolution. Two geoelectrical techniques were used to monitor dissolution for comparison. Reactive transport simulations were then performed to determine the spatial and temporal distributions of the ion concentrations, which were then used to inform geoelectrical properties from petrophysical relationships.

2. Material and Method

This section is divided into two parts. First, we introduce the flow-through experimental setup, comprising the presentation of the column design, outlet water monitoring, geoelectrical monitoring, and experimental protocols. Second, we introduce the coupled numerical workflow that combines reactive transport simulation and petrophysical modeling.

2.1. Flow-through experimental setup

The full setup and the column are presented in Figure 1.

2.1.1. Column design

The column is a Plexiglas cylinder with a length of 31 cm and an inner diameter of 4 cm (Figure 1b). The dimensions of the column and electrode

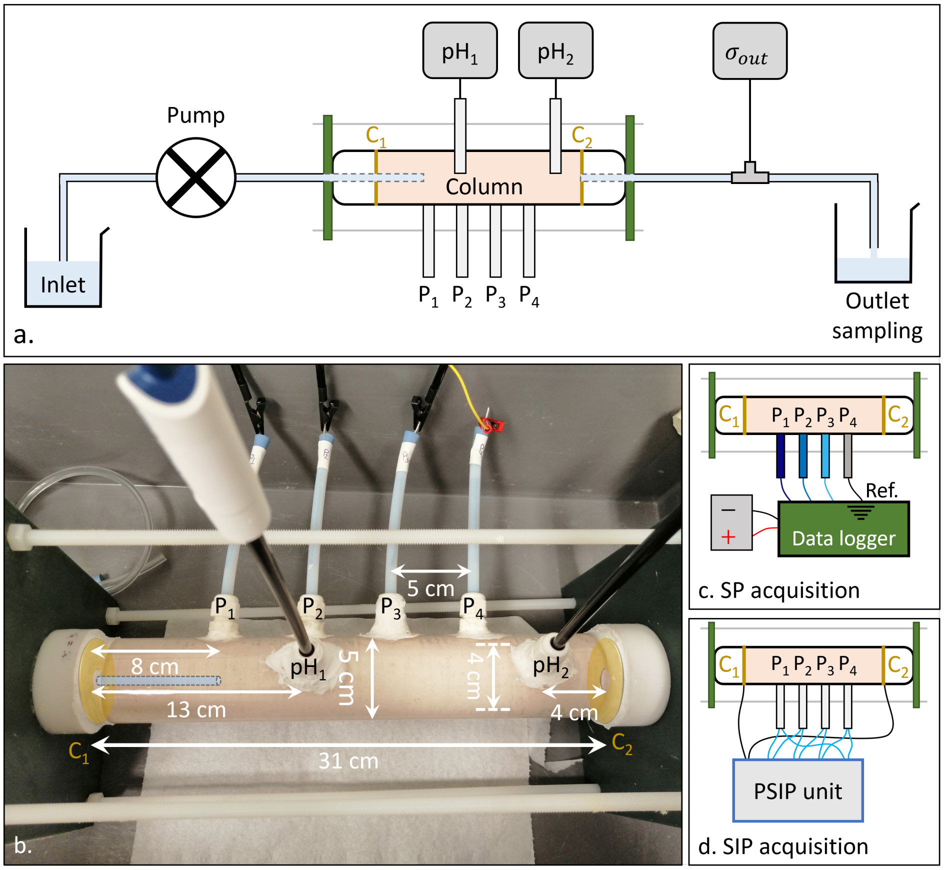

Figure 1: (**a**) The experimental set-up. (**b**) The column and its dimensions. Schematic shifted injection and current electrodes are shown in transparency. (**c**) SP acquisition. (**d**) SIP acquisition.

spacing have been set to respect the geometrical criteria recommended by Zimmermann et al. (2008) to ensure good quality of electrical acquisition. The column is sealed at each extremity by two plastic caps maintained with silicone joints and a tightening structure made of nylon. Plastic materials are used for this structure, instead of metallic components, because the latter would cause interference during geoelectrical acquisition. A filter fabric with a mesh of 20 µm is placed between the Plexiglas cylinder and the plastic cap at the column outlet to retain the grains in the column. C_1 and C_2 are the electrodes for electric current injection. They are two stainless steel perforated discs placed between the extremities of the Plexiglas cylinder and the sealing plastic caps. For electrical connection, the plastic caps are drilled to thread and glue stainless steel wires. P_1, P_2, P_3, and P_4 are the electrodes for electric potential measurement. They are spaced by 5 cm between them and 8 cm from C_1 and C_2. At the inlet, the injection tube is inserted in the column 8 cm after the entrance. It corresponds to the location of P_1. As recommended by Petiau and Dupis (1980), P_1 to P_4 electrodes are silver–silver chloride (Ag–AgCl) electrodes given the low noise and short stabilization time of this electrode type (e.g., Jougnot and Linde, 2013).

Pure calcite was used for the porous media in the flow-through columns. Loose calcite grains were obtained from crushed high-purity ($>99\,\%$) marble (Durcal 130 from Omya). Since the initially crushed calcite contains a wide variety of grain sizes, it is sieved to extract a range of grain diameters between 125 and 250 µm. The initial porosity ϕ_{init} ($-$) is calculated by weighing the mass of calcite required to fill the entire column volume. The final porosity ϕ_{end} ($-$) is calculated using the same method from the mass of calcite recovered in the column at the end of the experiment and after being dried in an oven. The porosity increase $\Delta\phi$ ($-$) is calculated from the initial and final porosity difference. The time variations of the porosity ϕ ($-$) are retrieved from the mass of dissolved calcite, obtained from the calcium concentration measurements on the collected outlet water samples. Both methods are compared at the end of the experiment.

Two pH electrodes (pH Sensor InLab Flex-Micro from Mettler Toledo), labeled pH_1 and pH_2, are inserted in the column at 13 and 27 cm, respectively. The pH meters (Lab 845 from SI Analytics) record measurements every 5 min.

2.1.2. Outlet pore water monitoring

A conductivity meter (Lab 945 from SI Analytics) was connected to conductivity flow-through measuring cells (TetraCon DU/T from WTW) to monitor water conductivity at the outlet (σ_{out}) every 5 min. Samples of outlet water were collected, with a sampling rate comprised between 30 min and 1 h, to monitor the chemical evolution through time. pH and conductivity are measured immediately after sampling. Then, the samples were filtered (< 0.2 μm) and split into two aliquots. The first aliquot was used to measure the total alkalinity through standard acid/base titration and corresponds to the concentration of alkaline species present in the solution, bicarbonate (HCO_3^-), carbonate (CO_3^{2-}), and hydroxide (HO^-) ions. The second aliquot was used to measure concentrations of major ions (calcium Ca^{2+}, chloride Cl^-, sodium Na^+, potassium K^+, magnesium Mg^{2+}, and sulfate SO_4^{2-}). Anions were measured using an ion chromatography system (from Dionex, 10% of global uncertainty), while cations concentrations were generated from inductively coupled plasma atomic emission spectroscopy (ICP-OES 5100 from Agilent technologies, 5% of global uncertainty).

2.1.3. Geoelectrical monitoring

The self-potential (SP) method is based on the passive measurement of the electrical field that results from the electrical current generated by different natural contributions (e.g., Jouniaux et al., 2009; Revil and Jardani, 2013). In this study, SP data are recorded with the total field method (Lowrie and Fichtner, 2020). The electrode P_4 is the reference (Figure 1c). The potential difference is measured for the three electrodes P_1, P_2, and P_3. The data logger is a CR1000 from Campbell Scientific. It is programmed to measure the voltage every 1 ms, then to compute and record a mean value every 5 s. Despite the rejection of 50 Hz, the mains frequency, the high level of noise compared to the amplitude of the SP variations requires filtering the data. Thus, the SP signal is filtered using a moving average window of 10 min, thus, averaging 120 measurements on each time window.

The spectral induced polarization (SIP) method, by injecting an alternating current at a low-frequency range (typically from mHz to kHz) (e.g., Revil et al., 2012a), measures both the sample's electrical conductivity and the ability of the porous rock to polarize (e.g., Binley and Slater, 2020). An alternating electric current I^* (A) is injected through the current electrodes C_1 and C_2. The resulting voltage V^* (V) is measured simultaneously on four channels between pairs of the Ag-AgCl electrodes P_1, P_2, P_3, and P_4 (Figure 1d). To be able to monitor the SIP signal of different slices of the column, we measure on pairs P_1–P_2, P_2–P_3, and P_3–P_4. We also measure the SIP response on pair P_1–P_4 to get the overall behavior. The SIP measurements are conducted using a PSIP device from Ontash and Ermacs (www.ontash.com), designed for multi-pair acquisition. The alternating voltage covers a spectrum from 5 mHz to 10 kHz at 40 frequencies uniformly distributed on a logarithmic scale and with an amplitude of ±5 V. At each frequency ($f = \omega/2\pi$ in Hz), the device records the complex electrical conductivity $\sigma^* = I^*/(k_G\, U^*)$, where k_G (m) is the geometrical coefficient determined using numerical simulation accounting for the acquisition geometry and the shape of the electrodes, thus, the electrical conductivity is independent of the electrode configuration. In this study, we use EIDORS (Electrical Impedance and Diffuse Optical tomography Reconstruction Software) for the 3D reconstruction of the electrical impedance tomography based on finite-elements numerical models (Rembert, 2021). We estimate $k_G = 2.5$ cm for the pairs P_1–P_2, P_2–P_3, and P_3–P_4 and $k_G = 0.8$ cm for the pair P_1–P_4.

2.1.4. Experimental protocols

Initial conditions and duration for all experiments conducted are listed in Table 1.

For all experiments, the column is filled with packed calcite grains and a saturating solution meant to be at saturation with calcite using the same technique (Rembert, 2021). The initial saturating solution is a mixture of deionized water and calcite grains immersed for several weeks. Despite the long mixing time between the grains and the water before filling the column, we systematically recorded an increase in the outlet water conductivity after a few hours in contact with the grains in the column. Thus, after closing it, the column was flushed for 24 h and the conductivity of the outlet water was recorded to check that it returned to its base value. Only for experiment ④, this procedure was shorter, resulting in some initial fluctuations in the outlet water conductivity presented in the results.

In this study, the dissolution of calcite is induced by the injection of different acid solutions to characterize the impact of strong or weak acids.

Table 1: Experimental conditions of the five experiments.

Experiment	①	②	③	④	⑤
Inlet acid	HCl	$CH_3CO_2H^a$ + $NaCH_3CO_2$	$CH_3CO_2H^b$ + $NaCH_3CO_2$	HCl	CH_3CO_2H
pH_{inlet}	4.5	4.5	4.5	3	2.5
Duration (h)	25	9	9	50	25
Electrical method	SP	SP	SP	SIP	SIP
Flow rate (mL h^{-1})	11	25	11	11	25
ϕ_{init} (%)	43.61	43.99	41.62	43.24	45.70
$\Delta\phi$ (%)	0.04	0.77	0.09	0.04	4.12

$^aC_{CH_3CO_2H}$ =1.74 mol L^{-1}

$^bC_{CH_3CO_2H} = 2.5 \times 10^{-3}$ mol L^{-1}

Strong acids completely dissociate in water. Thus, the pH value is directly linked to the concentration of acid and induces highly localized dissolution (e.g., Garcia-Rios et al., 2014; Rembert et al., 2022). Hydrochloric acid (HCl) was chosen as our representative strong acid, consistent with prior studies (① and ④) and the chemistry of the electrodes that can release Cl^- ions. The inlet solutions were prepared from the dilution of a commercial solution with an initial concentration of 36.4 %.

For experiments ②, ③, and ⑤, solutions of acetic acid (CH_3CO_2H), buffered or not with sodium acetate ($NaCH_3CO_2$), representative for weak acid, are injected. The aim of using such different acid types is to observe the effect of local versus extended reactive zones in the column on the geoelectrical signal. Buffering the acetic acid with acetate enables further expansion of the reactive zone (e.g., Garcia-Rios et al., 2014). The inlet solutions were prepared from Normapur products with guaranteed 99 % purity.

The experiments were conducted at room temperature. The room temperature was regulated by an air-conditioning system (20 ± 0.9 °C). Inlet acid injection was ensured through a peristaltic pump. The constant flow rate was set to 11 or 25 mL h^{-1}. Given the dimensions of the column (radius $r = 2$ cm) and the initial porosity range, this leads to pore velocities $V = Q/(\pi r^2 \phi)$ of $V_1 = 2.0$ cm h^{-1} and $V_2 = 4.4$ cm h^{-1}, respectively. The microscopic Péclet number is defined as

$$Pe = \frac{V\,\overline{d_g}}{D}, \tag{1}$$

where $\overline{d_g} = 188$ µm is the mean grain diameter and $D = 3.0 \times 10^{-9}$ m^2 s^{-1} is a mean diffusion coefficient. The Péclet numbers calculated from Darcy velocities U_1 and U_2 correspond to 0.35 and 0.75, respectively. $Pe < 1$ is set in the experiments, leading to a relatively dominant diffusion regime (Fredd and Miller, 2000). The Péclet number definition at diffusion scale is used rather than the dispersion one to investigate the impact of diffusion on the chemical reaction. In order to grasp the flow regime over the scale of the column, we calculate the macroscopic Péclet number

$$Pe_{macro} = \frac{U\,L}{Disp}, \tag{2}$$

where $L = 23$ cm is the length of the column from the location of the injection to the outlet, $U = \phi V$ is the Darcy velocity, and $Disp = \alpha U$ (m^2 s^{-1}) is the lateral dispersion coefficient, and α (m) is the dispersivity length scale, corresponding to the radius of the column, $R_{column} = 2$ cm. Thus,

$Pe_{macro} = L/\alpha = 11.5$. This value, suggests that we are in an advective regime with low velocity differences between the center of the column and the borders. Therefore, a 1D approximation to model the column is a valid approach.

2.2. Modeling approach

Coupled petrophysical, hydrological, and geochemical parameters are necessary to resolve the petrophysical modeling. Thus, a modeling workflow is used to predict the geoelectrical response (Figure 2) based on the developments from Rembert et al. (2022). The workflow combines reactive transport simulation with petrophysical modeling to predict the porosity, electrical conductivity, formation factor, and electro-diffusive contribution. to relate geoelectrical acquisition both to pore water chemical composition and porous structure.

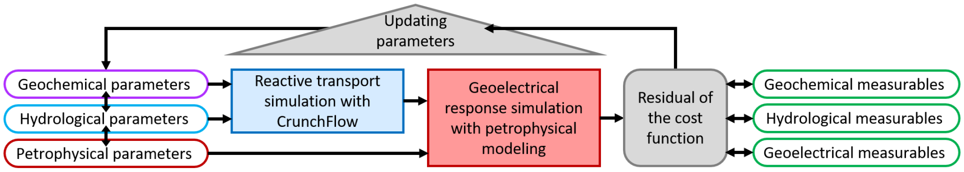

Figure 2: Workflow for the spatial and temporal quantitative characterization of the transport and reaction of solutes from the prediction of geochemical, petrophysical, and geoelectrical properties using reactive transport simulation and petrophysical modeling.

2.2.1. Reactive transport simulation

Each experiment was simulated using CrunchFlow, a robust multicomponent reactive transport modeling software developed by Carl Steefel and coworkers (Steefel, 2009). The code is based on a finite volume discretization of the governing coupled partial differential equations linking flow, solute transport, multi-component equilibrium, and kinetic reactions in porous media as follows (e.g., Molins et al., 2014; Garcia-Rios et al., 2014),

$$\frac{\partial}{\partial t}(\phi\, C_i) = \nabla \cdot (\phi\, \boldsymbol{D}_i \nabla(C_i) \,-\, q\, \phi\, C_i) \,-\, \sum_{r=1}^{N_r} v_{ir}\, R_r \,-\, \sum_{m=1}^{N_m} v_{im}\, R_m, \qquad (3)$$

where C_i (mol kg^{-1}) represents the total concentration for a given primary species i in the aqueous phase and ϕ is the total porosity of the porous medium ($\mathrm{m^3}_{\mathrm{void}}\ \mathrm{m^{-3}}_{\mathrm{porous\ medium}}$). The mass accumulation rate $\frac{\partial}{\partial t}(\phi\, C_i)$ is described by the combined dispersion-diffusion tensor $\boldsymbol{D}$ (m^2 s^{-1}), advection through the Darcy flow velocity vector q (m s^{-1}), and reactivity shown here as two summations accounting for kinetically controlled homogenous, aqueous (designated with subscript r) and heterogenous, mineral (designated with subscript m) reactions.

The advection-reaction-diffusion equation (ARDE) is resolved. We use CrunchFlow to simulate spatial and temporal distributions of aqueous species during calcite dissolution. The different values are set in the input file and the input conditions are summarized in Table 2. The porous medium is set as pure calcite ($CaCO_3$). For all simulations, the initial pore water is considered at equilibrium with calcite, and the inlet solution composition is set to correspond to the injected acid solutions described above. The reaction considered in the model is the dissolution of calcite and the speciation of carbonates. The kinetic rate and equilibrium constant come from Palandri and Kharaka (2004) and Plummer and Busenberg (1982), respectively. A neutral, linear reaction mechanism (pH 7) was chosen to describe calcite dissolution rates given the relatively elevated pH and low P_{CO_2} ($\approx 7 \times 10^{-4}$

atm) starting conditions for the experiments (Plummer et al., 1978; Chou et al., 1989; Pokrovsky et al., 2005), which alleviates H^+ dependence (Sjöberg and Rickard, 1984). Further, sensitivity analyses for calcite dissolution rate mechanisms show little sensitivity in the reactive transport model to the choice of rate mechanism under the conditions of the experiments and time durations (one example is shown in Figure S.1 in Supp. Inf.). The specific reactive surface area is initially calculated based on the literature which uses a smooth, spherical grain approximation to determine the effective surface area (Mito et al., 2013; Beckingham et al., 2016), then it is updated following a shrinking sphere approximation for dissolution (Lichtner, 1996; Steefel and Lichtner, 1998),

$$A_m = A_{m,0} \left(\frac{\phi_t}{\phi_0} \right)^{2/3} \left(\frac{\phi_{m,t}}{\phi_{m,0}} \right)^{2/3}, \tag{4}$$

where $A_{m,0}$, ϕ_0, and $\phi_{m,0}$ are the initial surface area ($\mathrm{m^2}_{\mathrm{calcite}}\ \mathrm{m^{-3}}_{\mathrm{porous\ medium}}$), initial total porosity ($\mathrm{m^3}_{\mathrm{void}}\ \mathrm{m^{-3}}_{\mathrm{porous\ medium}}$), and the initial mineral volume fraction ($\mathrm{m^3}_{\mathrm{calcite}}\ \mathrm{m^{-3}}_{\mathrm{porous\ medium}}$), respectively. The total porosity and mineral volume fraction at the current time step are designated as ϕ_t and $\phi_{m,t}$, respectively, and are individually tracked in the model through mass-balance (Lichtner, 1996; Steefel and Lichtner, 1998),

$$\phi_{m,t} = \phi_{t-\Delta t} + V_s\, R_{calcite}\, \Delta t \tag{5}$$

and

$$\phi_t = 1 - \sum_{m=1}^{N_m} \phi_{m,t}, \tag{6}$$

where Δt is the current time step size, $t - \Delta t$ corresponds to the previous time step, V_s the calcite molar volume (3.69×10^{-5} $\mathrm{m^3}_{\mathrm{calcite}}$ $\mathrm{mol^{-1}}_{\mathrm{calcite}}$), and $R_{calcite}$ is the calcite reaction rate ($\mathrm{mol}_{\mathrm{calcite}}$ $\mathrm{m^{-3}}_{\mathrm{porous\ medium}}$ $\mathrm{s^{-1}}$).

The column is treated as a 1D porous medium. It is discretized with a regular mesh size $\Delta x = 1$ cm, except over 3–13 cm range, where the mesh size varies between 0.1 and 1 cm (Figure S.2 in Supp. Inf.). This leads to setting the longitudinal dispersion of 0.09 cm to not exceed the size of the smallest mesh (0.1 cm). Ionic species present in the solution have specific diffusion coefficients (Table S.1 in Supp. Inf.). The Debye-Hückel model for the activity coefficients is used in the model despite the ionic strengths of initial solutions in some experiments being sufficiently high for a Pitzer model treatment. This choice in the specific-ion interaction model can be justified in two ways. First, the Pitzer model is currently not implemented in Crunchflow (Steefel et al., 2015). Second, the Debye-Hückel model is sufficient to characterize ionic interactions for this particular Crunch model and the conditions of this study where aqueous concentrations are dominated by $\mathrm{Ca^{2+}_{(aq)}}$ and $\mathrm{HCO^{-}_{3\,(aq)}}$ and have low concentrations of $\mathrm{SO^{2-}_{4\,(aq)}}$ and $\mathrm{Mg^{2+}_{(aq)}}$ –both of which are main inhibitors of calcite dissolution (Morse et al., 2007). Additionally, experimental investigations into calcite dissolution rate dependence on ionic strength have demonstrated negligible dependence on total dissolved solids (TDS) at $\mathrm{pCO_2}$ values less than or equal to 0.1 bar (Gledhill and Morse, 2006; Finneran and Morse, 2009).

Table 2: Input conditions used in the numerical simulations.

Mineral	Calcite
Reaction stoichiometry	$CaCO_{3_{(s)}} + H^+ \rightarrow Ca^{2+} + HCO_3^-$
Equilibrium constant K_{eq} (log10)	1.8487†
Reaction kinetics k (log10, mol m^{-2} s^{-1})	-5.81‡
Specific surface area (m^2 g^{-1})	1.15*
Cementation exponent m	1.78
Longitudinal dispersivity (m)	9×10^{-4}

† Plummer and Busenberg (1982)

‡ Palandri and Kharaka (2004)

* Beckingham et al. (2016)

2.2.2. Petrophysical modeling

The modeled electrical signals are obtained from CrunchFlow reactive transport numerical simulation and the petrophysical relationships presented in this section. Thus, relating the electrical response to the geochemical, hydrological, and petrophysical parameters.

The water conductivity is computed from (e.g., Atkins and de Paula, 2014; Revil and Linde, 2006; Jougnot et al., 2010)

$$\sigma_w = \mathcal{F} \sum_i |z_i| \, \beta_i \, \gamma_i \, C_i, \tag{7}$$

where z_i (–), β_i (m^2 s^{-1} V^{-1}), γ_i (–), and C_i (mol m^{-3}) are the valence, the mobility, the activity coefficient, and the concentration of each ionic species i, respectively, and $\mathcal{F} \approx 9.65 \times 10^4$ C mol^{-1} is the Faraday constant.

The ionic concentration value comes from the reactive transport numerical CrunchFlow simulations. Applying Equation 7 to compute the outlet water conductivity enables assessing the quality of the simulations when compared to the measured electrical conductivities.

The SP method is simple to set up but complex to interpret as it involves the superposition of different possible sources of current (e.g., Hu et al., 2020). Among the contributions, reactive transport can be linked to two potential couplings: electrokinetic and electrochemical. First, the electrokinetic coupling is the generation of a streaming potential from water flow in the pores. Due to the presence of electric charge at the surface of minerals, the pore water carries an excess charge that generates the so-called streaming current (e.g., Quincke, 1859; Revil and Leroy, 2004; Jougnot et al., 2020; Soldi et al., 2020). Second, the electrochemical coupling called the electro-diffusive potential, is associated with ion concentration gradients that generate separation charge due to the difference of mobilities between migrating dissolved ionic species (e.g., Revil, 1999; Maineult et al., 2004; Revil and Linde, 2006; Mao et al., 2015; Rembert et al., 2022). Therefore, the interest of the SP method is that it allows the study of mixing and reaction zones between fluids as saline intrusions (e.g., Maineult et al., 2005; MacAllister et al., 2018; Graham et al., 2018) or water intrusion into hydrocarbon reservoir (e.g., Murtaza et al., 2011). We performed several tests on the considered material showing that the electro-diffusive contribution is dominating the SP signal compared to electrokinetic coupling when studying calcite dissolution even when we tested measuring SP variations in advection dominating regime with various fluid velocities, dissolution rates, and electrodes spacing (Rembert et al., 2022). This result comes from the low surface charge of calcite mineral and the impact of the water electrical conductivity which decreases the thickness of the EDL. The electro-diffusive contribution to SP voltage for the measuring electrode P_j (with j = 1–3) and the reference electrode P_4 is modeled as

$$\Delta V_{\mathrm{P}_j-\mathrm{P}_4} = \frac{\mathcal{R}T}{\sigma_w} \sum_i \frac{z_i}{|z_i|} \, \beta_i \, \gamma_i \, (C_{i,P_j} - C_{i,P_4}), \tag{8}$$

where $\mathcal{R} \approx 8.314$ J mol^{-1} K^{-1} is the molar gas constant and T (K) is the absolute temperature. Since the water conductivity is not measured in the column, σ_w is computed from Equation 7.

The complex electrical conductivity is expressed as

$$\sigma^* = \sigma^{'} + i\sigma^{''}, \tag{9}$$

where $\sigma^{'}$ is the real part and $\sigma^{''}$ is the imaginary part of the complex electrical conductivity. The real conductivity $\sigma^{'}$ corresponds to the electrical conduction in the porous medium. This term is related to the lithology, rock structure, water content, and solute concentrations (e.g., Rembert et al., 2023a). It is defined as follows

$$\sigma^{'} = \frac{\sigma_w}{F} + \sigma_s, \tag{10}$$

where F is the formation factor of the rock sample and σ_s is the surface conductivity of the minerals. In the case of calcite and considering the pore water electrical conductivities of this study, σ_s is negligible. Thus, the formation factor F is defined as follows

$$\lim_{\sigma_s \to 0} F = \frac{\sigma_w}{\sigma^{'}}. \tag{11}$$

The equation of Archie (1942) relates the formation factor to the porosity as follows

$$F = \phi^{-m}, \tag{12}$$

where m (–) is the cementation exponent. From SIP measurement on the column saturated with the initial solution of known conductivity, we inferred that $m = 1.78$. Using suitable $F - \phi$ relationships is an important topic in petrophysics. The power law described in Archie (1942) is the most famous and widely used relationship. However, its use is inappropriate for a strong dissolution regime (e.g., Niu and Zhang, 2019) but has proven its relevance for a lower one (e.g., Bernard et al., 2007). The imaginary conductivity $\sigma^{''}$ is associated with polarization phenomena. In the frequency range studied, the polarization results from the transient reorganization of an excess of charges in the so-called electrical double layer (EDL) at the surface of charged minerals. The structure of the EDL comprises the thin Stern layer coated by the wider diffuse layer (e.g., Heberling et al., 2011). The EDL polarization is frequency-dependent and is related to relaxation times, associated with characteristic lengths in the porous medium (e.g., pore length, pore aperture, grain size, roughness Leroy et al., 2008, 2017; Kemna et al., 2012; Revil et al., 2012b). Surface complexation reactions driven by mineral dissolution and precipitation processes can modify the mineral surface state and also influence the imaginary conductivity spectrum (e.g., Wu et al., 2010; Izumoto et al., 2022; Rembert et al., 2023b). This component of the complex electrical conductivity is not modeled with this workflow.

3. Results and Discussion

This section summarizes results for the five calcite dissolution flow-through experiments and associated modeling. It is organized by data type. For all experiments, time zero corresponds to the beginning of the reactive solution injection.

3.1. Outlet water chemistry

Outlet water concentrations as a function of time are presented in Figure 3. Initial values are consistent across all five experiments since the column is initially saturated with the same solution in thermodynamic equilibrium with calcite (mean saturation index $\mathrm{SI} = \log_{10}(Q/K) =$ -0.08, where Q is the ion activity product). For each experiment, aqueous species show synchronous variations between them corresponding to the arrival of the acid front at the outlet of the column. Curves obtained from numerical simulations are also plotted and show good agreement with the experimental data.

Experimental data and simulation curves of alkalinity and calcium concentration show an increase for experiments ②, ③, and ⑤. Calcite dissolution due to acetic acid injection adds calcium ions to the solution. For experiments ② and ③, sodium increases due to the presence of sodium acetate

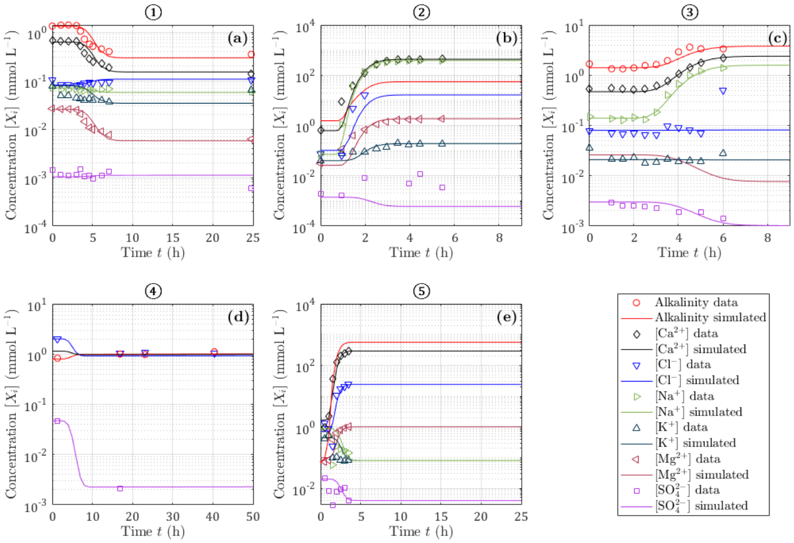

Figure 3: Experimental data and curves from 1D reactive transport numerical simulation of bicarbonate ($HCO_3{}^-$), (calcium Ca^{2+}, chloride Cl^-, sodium Na^+, potassium K^+, magnesium Mg^{2+}, and sulfate SO_4^{2-}) for (**a**) experiment ①, (**b**) experiment ②, (**c**) experiment ③, (**d**) experiment ④, and (**e**) experiment ⑤.

in the inlet solution to buffer the acetic acid. Reached values of alkalinity and calcium concentration are lower for experiment ③, due to lower acid concentration. Higher calcium concentrations are reached for experiment ② compared to experiment ⑤ while acid solutions have pH values of 4.5 and 2.5, respectively.

For the experiment ①, corresponding to hydrochloric acid injection at pH 4.5, alkalinity and calcium concentration decrease but do not fall to zero. The injected acid solution does not contain any calcium or bicarbonate ions, thus, the reached stable values indicate dissolution. In experiment ④, corresponding to hydrochloric acid injection at pH 3, alkalinity and calcium curves show a plateau with higher values compared to experiment ①.

3.2. pH monitoring

pH values recorded in the column (pH_1 and pH_2) and measured on the collected samples of outlet pore water (pH_{sample}) are displayed for all experiments in Figure 4. The experimental data pH_1, pH_2, and pH_{sample} are consistent with one another. For each experiment, the variations of pH_1, pH_2, and pH_{sample} follow similar trends with an increasing time delay consistent with the propagation of the acid front through the column. Simulation curves of pH_1, pH_2, and pH_{sample} are also displayed and show fairly good agreement with the experimental data.

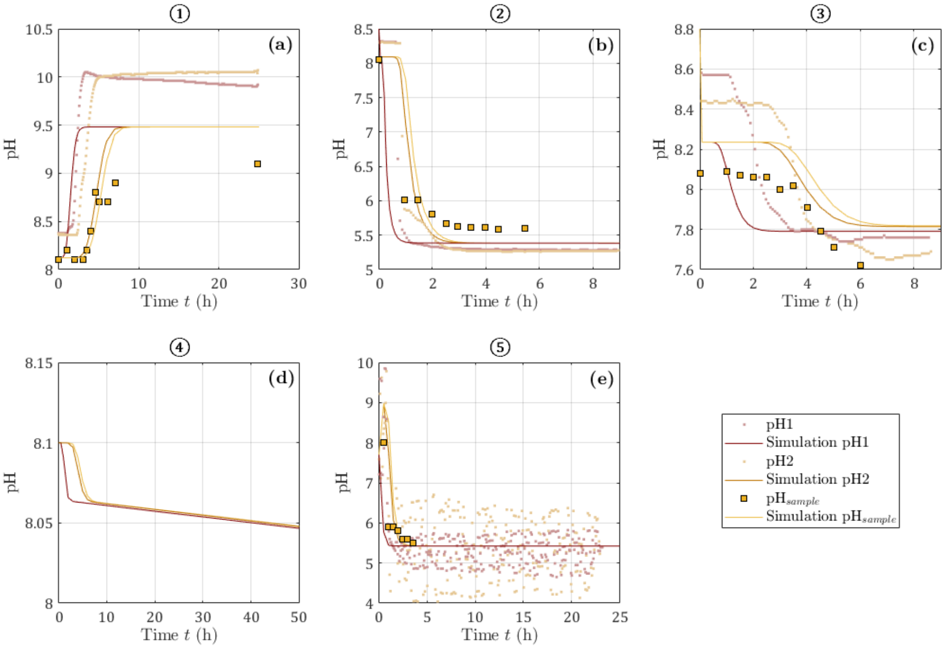

Figure 4: Experimental data and curves from 1D reactive transport numerical simulation of pH for (**a**) experiment ①, (**b**) experiment ②, (**c**) experiment ③, (**d**) experiment ④, and (**e**) experiment ⑤. pH_1 and pH_2 correspond to pH at 13 and 27 cm in the column, respectively. pH_{sample} comes from the collected samples of outlet pore water. For experiment ④, pH_1 and pH_2 were not measured. For experiment ⑤, pH_1 and pH_2 are noisy because of electric current injection for SIP acquisition, thus, envelopes of the data are displayed for clarity.

The smooth variations of pH_1 and pH_2 for experiments ①, ②, and ③ are results of high-precision monitoring. When SIP measurements are performed during experiment ⑤, the injection of electric current generates noise that is higher for pH_2, located close to the current electrode C_2. However, the simulated curves are centered with the envelopes of the experimental data, showing the consistency of the numerical simulation.

For experiments ① and ③, pH_{sample} is shifted in amplitude compared to pH_1 and pH_2, while it is not visible for the experiments ② and ⑤. During experiments ② and ⑤, a mixture of gas bubbles and pore water was observed at the outlet of the column. The gas bubbles are CO_2 bubbles that form due to the intense dissolution of calcite (e.g., Choi et al., 1998, photos of the columns at the end of each experiment are displayed in Figure S.3 in Supp. Inf.), as observed from the important production of Ca^{2+} ions. Indeed, CO_2 is produced by the high concentration of carbonic acid H_2CO_3, which is the soluble form of dissociated ions bicarbonate HCO_3^- and carbonate CO_3^{2-} in acid conditions. The experiments are conducted at atmospheric pressure, which induces the release of gaseous CO_2 (e.g., Rembert et al., 2023b). Thus, the amplitude shift of pH_{sample} may come from the late degassing of CO_2 after the pore water reaches the outlet of the column in the case of experiments ① and ③.

Except for experiment ①, pH values decrease with acid injection. For experiment ①, after pH_2 has risen to the same value as pH_1, pH_2 remains stable, while pH_1 constantly decreases until the experiment is stopped. For experiment ④, pH_1 and pH_2 were not monitored, and the values from the samples of outlet pore water present a low decrease. For experiment ③, compared to experiments ② and ⑤, the decrease in pH is less important, indicating weaker dissolution, which is consistent with the lower acetic acid concentration in the inlet solution. These results are also consistent with the measurements of the porosity difference (Table 1), showing that more calcite has been dissolved in experiments ② and ⑤ compared to experiment ③.

3.3. Outlet water conductivity

Outlet water conductivity measured values and simulated curves are plotted for all experiments in Figure 5. The outlet conductivity monitored with the in-line conductivity meter is named σ_{out}. The conductivity of the sampled outlet pore water σ_{sample} is also displayed except for experiment ④, for which it was not measured. Both measurements are in accordance except for experiments ② and ⑤, for which σ_{out} is unreliable due to CO_2 degassing that creates partial saturation in the tubes and bad detection with the in-line conductivity meter. Therefore, comparing the measured σ_{sample} with the modeled curve is preferred in this case.

Comparable initial conditions were set between the experiments with similar initial values comprised between 100 and 150 $\mu S\ cm^{-1}$, except for experiment ④, where problems of initial solution injection cause fluctuations synchronous with ion concentration data and corresponding to the acid front's arrival at the column outlet. Calcite dissolution is expected to increase the conductivity of the outlet water over time by adding dissolved ionic species (e.g., calcium) to the solution (e.g., Rembert et al., 2023a). This expected behavior is observed for experiments ②, ③, and ⑤, for which acetic acid is injected. On the contrary, for experiments ① and ④, hydrochloric acid

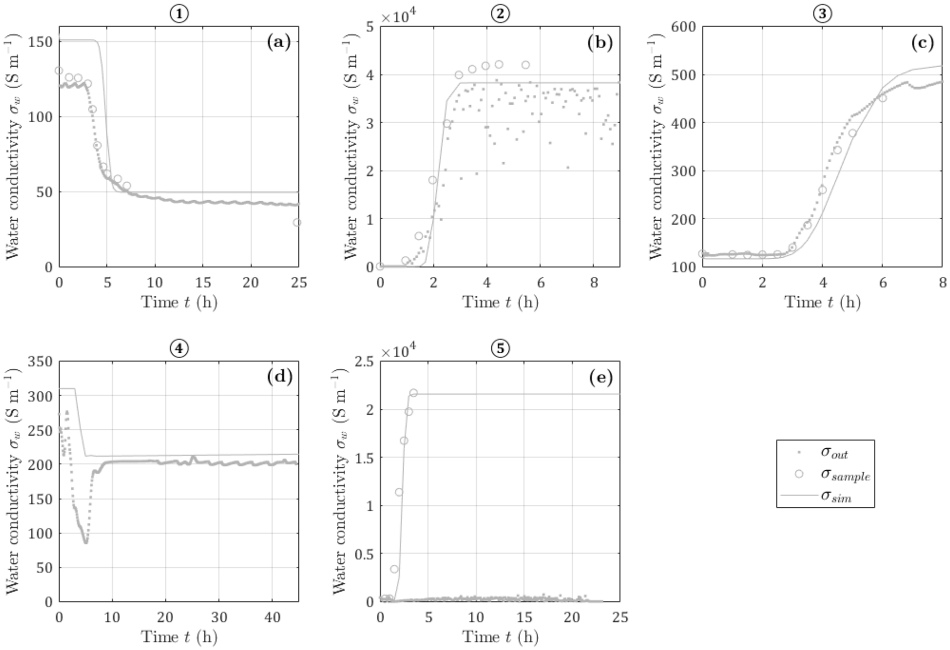

Figure 5: Outlet water conductivity, measured with the in-line conductivity meter (σ_{out}) and from the outlet water samples (σ_{sample}), and modeled with 1D reactive transport numerical simulation (σ_{sim}) for (**a**) experiment ①, (**b**) experiment ②, (**c**) experiment ③, (**d**) experiment ④, and (**e**) experiment ⑤.

is injected, and σ_{out} decreases. This result is explained by the difference in ion concentrations and mobilities impacting the solution conductivity (e.g., Rembert et al., 2022). Indeed, the consumption of hydrogen ions (H^+) during the calcite dissolution decreases the water conductivity because H^+ ions have a much higher mobility compared to calcium or bicarbonate ions (by one order of magnitude). Small oscillations and hangings are visible on σ_{out} experimental data for experiments ①, ③, and ④. They are caused by the air-conditioning system for room temperature regulation.

The curves of the numerical simulations σ_{sim} show good agreement in dynamics and amplitudes for all of the experiments, while variable inlet acids and broad concentration ranges are used and still with σ_{sample} when there is CO_2 degassing.

3.4. Porosity, real electrical conductivity, and formation factor

The porosity, the formation factor, and the real electrical conductivity obtained from experimental data and reactive transport simulation for all of the experiments are presented in Figure 6.

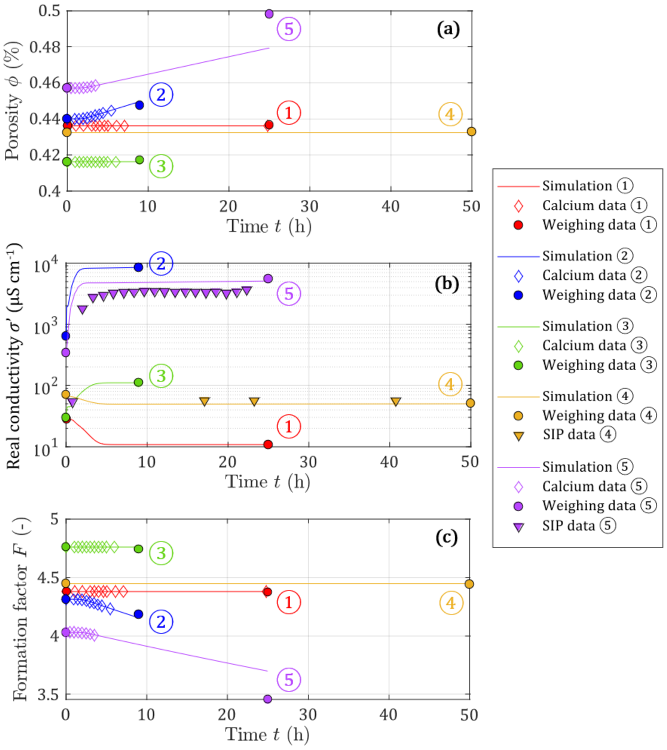

Figure 6: Experimental data and curves from 1D reactive transport numerical simulation of (**a**) porosity, (**b**) real electrical conductivity, and (**c**) formation factor for the five experiments. Porosity values are estimated from calcite grains weighing data (discs), measured calcium concentration (diamonds), and simulated (curves). The real electrical conductivity curves are determined from simulated porosities and simulated water conductivity using the model from Archie (1942). For experiments ④ and ⑤, the simulated electrical conductivities are confronted with the real electrical conductivity σ' measured with the SIP method.

Initial values of porosity estimated by weighing the mass of calcite filling the column are in the close range from 41.62 to 43.99 % (Table 1), showing that comparable initial conditions are set with the column-filling procedure used. For all experiments, the final porosity is higher, with an increase ranging from 0.04 to 4.12 %, and more important for experiments ② and ⑤. Time variations of the porosity are estimated from the monitoring (diamonds) and the simulation (curves) of calcium concentration in the samples of outlet pore water (Figure 6a). Porosity values estimated from calcium concentration show excellent correspondence between experimental data and simulated curves. Thus, porosity modeling from the simulated calcium concentration is accurate for most of the experiments. There is also a good agreement with the porosity values estimated from calcite grains weighing data. Even for experiment ⑤ since the difference corresponds to an error of 3.7 % of the final mass of calcite. For experiment ⑤, the porosity reaches a higher value from the weighing data. Nevertheless, the associated percentage of the error in this measurement is of 3.7 % of the final mass of calcite. This low error value can be associated with weighing procedure uncertainty.

The real electrical conductivity of the column is experimentally obtained from SIP measurements of $\sigma'_{\mathrm{P}_1-\mathrm{P}_4}(1\ \mathrm{Hz})$ for experiments ④ and ⑤. The real electrical conductivity of the column is also estimated from the porosity, based on the relationship of Archie (1942) for a constant cementation factor (Equations 11 and 12). The literature shows that this assumption is not valid for highly heterogeneous samples (e.g., Garing et al., 2014), and strong dissolution rates in advective regimes (e.g., Noiriel et al., 2004), but it verifies for lower ones (e.g., Niu and Zhang, 2019; Rembert et al., 2023a). In this study, the column is homogeneously filled with calcite grains and the flow regime is diffusion-dominated. For experiment ④, there is a strong agreement between the SIP measurements, the simulated curve, and the initial and final values determined from weighing data. For experiment ⑤, the agreement between the SIP measurements and the real conductivity determined from porosity data and simulations is less accurate, but of the same order of magnitude. These results highlight that Archie's equation is valid in these conditions of calcite dissolution in a homogeneous sample.

All experiments present real electrical conductivity variations consistent with the water conductivity evolution (Figure 4). Acetic acid injection (experiments ②, ③, and ⑤) increases the real conductivity, while it decreases for hydrochloric acid injection (experiments ① and ④).

The formation factor (Equations 11 and 12) describes the evolution of the pore space structure. As for the real electrical conductivity calculation, the formation factor is determined considering a constant cementation exponent. As previously documented in the literature, calcite dissolution is associated with a reduction in the formation factor (e.g., Rembert et al., 2020, 2023a). The formation factor curves exhibit a reverse relationship with the porosity curves.

3.5. SP and electro-diffusive modeling

SP measurements are presented in Figure 7a–c. They present similar patterns with bell-shaped variations that start first for the pair P_1–P_4, then P_2–P_4, and finally P_3–P_4, but end simultaneously. As documented in the literature (e.g., Maineult et al., 2004; Rembert et al., 2022) such SP signals with bell-shaped variations are generated by concentration gradients. Compared to the variations of pH monitored inside the column and the outlet measurement, the bell-shaped variations of SP signals are synchronous with the acid front propagation through the column. Furthermore, following the literature and the configuration of the electrodes, the positive or negative bell-shaped responses are consistent with the increase or decrease of σ_{in} due to the reacting solution injection. At the beginning of the experiment, the SP curves show very similar values for each pair of electrodes, despite their different distances from the reference electrode P_4. This is the opposite of what would be observed in the case of an electrokinetic source. Thus, there is no electrokinetic contribution as observed by Rembert et al. (2022), only the electro-diffusive contribution to SP values is considered.

Depending on the experiment, after the bell-shaped variation, some SP pairs return to their base value and remain stable. Thus, these pairs of electrodes are only affected by a transient source of SP current which is the ion concentration gradient caused by the acid front propagation. In contrast, other pairs reach stable values of different amplitude than initially. These changes in amplitude are related to permanent concentration gradients between the measuring electrode and the reference. For experiment ① (Figure 7a), after the bell-shaped variation, pair P_1–P_4 shows a stable value greater than 1 mV not observed for the other pairs. This is associated with the localization of the reaction zone between the electrodes P_1 and P_2. For experiment ② (Figure 7b), as the three curves show very close final values, it is likely that they all lie within the reactive zone. In addition, there is a noticeable pulse at $t = 1$ h and noticeable synchronous oscillations for all pairs

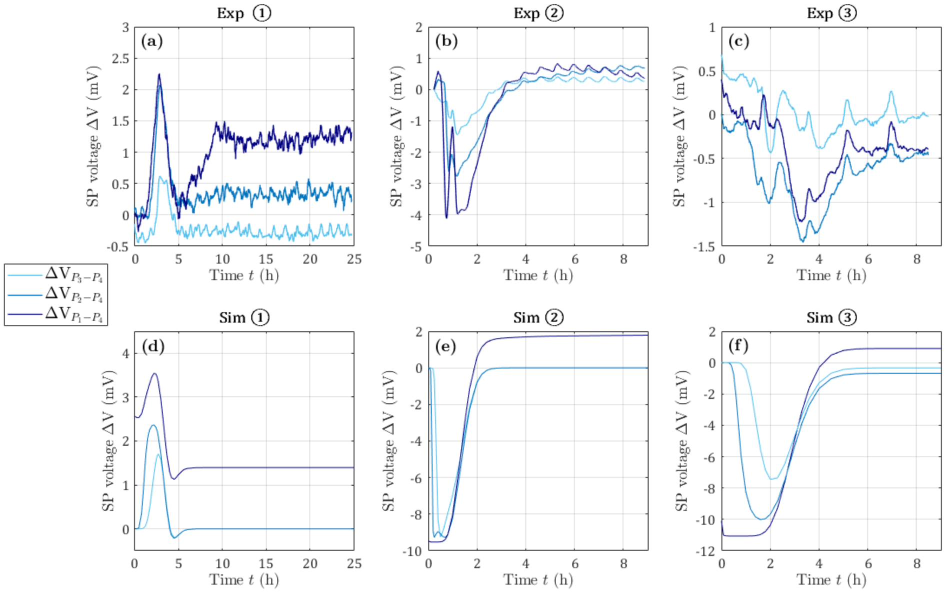

Figure 7: SP monitoring for (**a**) experiment ①, (**b**) experiment ②, and (**c**) experiment ③. The data are filtered with a moving average window of 10 min. Numerical simulations of the electro-diffusive coupling for (**d**) experiment ①, (**e**) experiment ②, and (**f**) experiment ③.

of electrodes related to the room temperature control with air conditioning. For experiment ③ (Figure 7c), the SP curves show negative variations of lower amplitude compared to the variations of experiment ②. This is consistent with the close conductivity values between the inlet acid and the initial solution. There are also some pulses due to room temperature regulation.

The numerical results are displayed in Figure 7d–f. The curves show good agreement with the measurements regarding the sign and time evolution of the bell-shaped variations. The amplitudes are of similar magnitude for experiment ① with hydrochloric acid injection. On the contrary, SP is overestimated for acetic acid injection in experiments ② and ③ with an order of magnitude difference. This difference in magnitude is linked to the acid type. In the case of hydrochloric acid injection, H^+ ions dominate the diffusion and are simpler to model. However, when injecting acetic acid multiple species are competing, thus, the concentration gradient is more complex to model. Since the workflow puts modeling results in series, the inaccuracies accumulate when modeling SP response. In addition, the model is 1D neglecting 3D effects, which are discussed later.

Nevertheless, compared to physicochemical monitoring, SP variations during calcite dissolution show that the spatialization of the reactive zone can be revealed with this method. In comparison, pH electrodes inserted in the column do not provide this information, except for experiment ①, for which the slight decrease of pH_1 reveals that the reactive zone reaches this location but does not affect pH_2 similarly.

The modeling of the electro-diffusive contribution shows good agreement for the experiment ①, for which strong acid is injected. The results are less accurate for experiments ② and ③ with buffered acetic acid injection. From the outlet water conductivity results, the mobility of H^+ protons plays a major role when injecting hydrochloric acid. On the contrary, for acetic acid injection, other ionic species contribute extensively. This diversity of contributions complicates the modeling, even if it shows that the reactive zone is limited to P_1–P_2 range for experiment ①, while it is extensive to the outlet for experiments ② and ③.

3.6. Imaginary conductivity spectra

Figure 8 presents the imaginary conductivity spectra obtained for experiments ④ and ⑤ for the three pairs P_1–P_2, P_2–P_3, and P_3–P_4 over time.

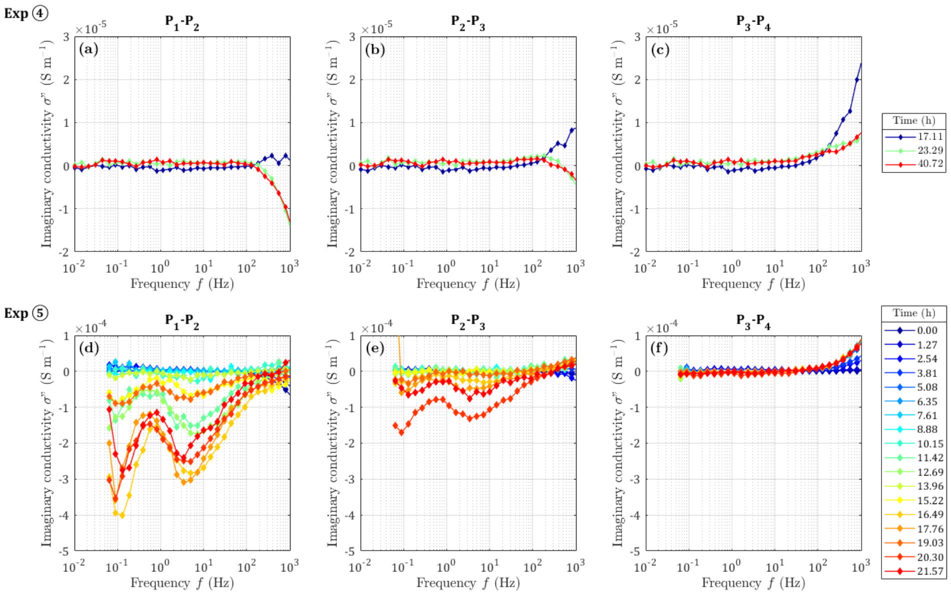

Figure 8: Imaginary conductivity spectra of pairs P_1–P_2, P_2–P_3, and P_3–P_4 at different times of (**a**, **b**, **c**) experiment ④ (S4, hydrochloric acid at pH=3) and (**d**, **e**, **f**) experiment ⑤ (acetic acid S5). Injections of S4 and S5 define the time zero of each experiment.

For experiment ④ (Figure 8a–c), imaginary conductivity spectra remain flat for all pairs during the entire experiment for frequencies below 500 Hz. For frequencies above 500 Hz, the successive pairs present three different trends. For P_1–P_2, imaginary conductivity values are negative, growing in absolute value, then stabilizing with time. For pair P_2–P_3, high-frequency imaginary conductivities are first positive, then they become negative, with lower amplitude in absolute value compared to high-frequency imaginary conductivities of pair P_1–P_2 for the same time. Imaginary conductivities of pair P_3–P_4 are always positive.

Experiment ⑤ presents similar patterns for high-frequency imaginary conductivities (Figure 8d–f), with important negative values for pair P_1–P_2, less negative values for pair P_2–P_3, and positive values for pair P_3–P_4. These negative imaginary conductivity have been seen in reactive media (Izumoto et al., 2022). In addition, there are two bell-shaped negative variations for frequencies below 500 Hz. These bumps are centered on 0.15 and 3.5 Hz. Similar peaks have been observed during calcite dissolution in Rembert et al. (2023b).

Imaginary conductivity spectra have contrasted variations between experiments ④ and ⑤. Values are close to zero for experiment ④ while there are remarkable variations for experiment ⑤ of acetic acid injection generating strong dissolution regime. In addition, negative values are measured for experiment ⑤. According to the theory, they are associated with a not expected inductive behavior. However, due to the strong dissolution regime, pH is decreased toward acidic conditions, where calcite surface charge may change sign (e.g., Eriksson et al., 2007; Heberling et al., 2021). Sign variation of the imaginary conductivity during precipitation and dissolution processes has already been reported in the literature (Izumoto et al., 2022; Rembert et al., 2023b) but is still difficult to interpret with the existing models. Thus, the results from this method do not show results as clear as SP monitoring and are harder to interpret. Besides, SIP is more difficult to conduct in the field compared to SP setup. Time-domain induced polarization (TDIP) may be another solution to investigate. Thus, for future field studies of reactive contamination, the authors recommend more investigations with the SP method.

3.7. Relationship between acid type and dissolution process

From the description of the results, the impact on calcite dissolution between chloride (strong) or acetic (weak) acid injections can be clearly distinguished. There are also contrasted results between buffered with sodium acetate and not buffered acetic acid solutions, with higher and lower concentrations of acetic acid. The numerical simulations can extract the distribution in space and time of the reaction rate. It is represented at 9 h after the start of acid injection in each experiment in Figure 9. From the outputs of the CrunchFlow models we can also get the value of the dissolution rate at the injection point. The values are summarized in Table 3. They highlight more dissolution for acetic acid solutions compared to hydrochloric acid solutions for the same pH. In addition, when looking at the spatial variations of the dissolution rate, we observe that it is more stable for experiments ② and ③ than for others, coming from the fact that they are buffered with sodium acetate (rate.out files archived on Zenodo.org).

Table 3: Dissolution rates at the injection point from CrunchFlow modeling at the first time step.

Experiment	①	②	③	④	⑤
Dissolution rate at the injection point ($\mathrm{mol\,m^{-3}\,s^{-1}}$) at 0.1 min after starting the injection.	$8.89\ 10^{-4}$	2.08	$1.46\ 10^{-2}$	$5.97\ 10^{-2}$	2.05

The impact of acid type can be seen in the extent of the reactive zone in the column. The expansion of the reactive zone is minimal for experiments with hydrochloric acid injection (① and ④), and broader for experiments with acetic acid injection (②, ③, and ⑤). Despite a low concentration of acetic acid for the experiment ③, the reactive zone is extended from P_1 to

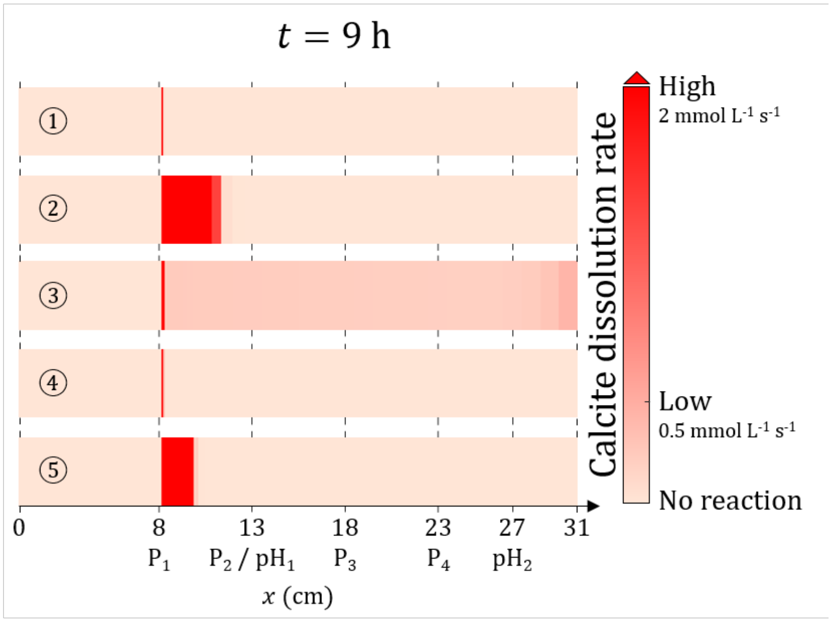

Figure 9: Reactive zone location for the different experiments of calcite dissolution from the dissolution rate extracted from the numerical simulations at 9 h after the start of acid injection for the five experiments. The same color scale is used for all of the experiments. The maximum value is set to 2 mmol L^{-1} s^{-1}, but the red color indicates values that can be higher.

the outlet of the column, opposite to the experiments with the hydrochloric acid injection of the same or lower pH. This spreading of the reactive zone when injecting acetic acid compared to hydrochloric acid is in agreement with the results of the literature (e.g., Garcia-Rios et al., 2014).

From experiments ② and ⑤, the reactive zone is more extended for experiment ②, while the inlet acid has a higher pH value (pH=4.5) compared to the injected acid in experiment ⑤ (pH=2.5). The inlet acid is a buffered solution of acetic acid with sodium acetate for experiment ②. From the porosity increase simulated after 9 h of acid injection, porosity has increased by a third more for experiment ② compared to experiment ⑤, showing that dissolution is more intense for experiment ②. Buffering the inlet acid increases the dissolution power.

3.8. Specific discussion about the reactive transport simulation

The experimental results presented in this study reveal that calcite dissolution does not exhibit a unique geoelectrical response, but rather distinct signatures that can be opposite, depending on the porous medium, inlet chemistry, and flow regime. Thus, addressing the reactivity using a sophisticated, robust treatment of reactivity through a reactive transport framework improves interpretations for geoelectrical signals compared to the use of empirical constants (Cherubini et al., 2019).

The strongest hypothesis in the model is to consider the column as a 1D system. This assumption is valid considering the small diameter of the base, although it is worth 13 % of the column length. Furthermore, the column is filled with well-sorted sieved grains of calcite, to ensure maximum homogeneity opposite to using consolidated limestone samples as in Rembert et al. (2023a), for which preferential dissolution pathways formed due to initial heterogeneity (Leger et al., 2022). The porous medium is considered an effective medium, where the formation of a preferential path is neglected. However, local heterogeneity of the flow through granular media is not a detail (e.g., Stevenson, 1997). Some additional 3D effects may arise from the column horizontal orientation and density difference between the injected acid and the initial saturating solution, especially for experiments ② and ⑤. For these two experiments, there is a density contrast $\Delta d > 0.02$ between the initial pore water and the injected acid solutions. It is known from the study of saline intrusions in coastal aquifers, that for such a density contrast, salt wedges form under the freshwater (e.g., Rattray and Mitsuda, 1974). This leads the injected acid solutions to flow preferentially in the lower half of the column before replacing the initial pore water. The good agreement between the sampled and the modeled outlet water conductivity is in favor of the replacement of the less dense water. This stratification induces calcite dissolution preferentially on the lower side of the column (Figure S.3 in Supp. Inf.). In addition, the production of CO_2 bubbles that accumulate in bigger pores and on the upper side of the column also influences the flow path. However, geoelectrical methods are integrative measurements, and sensitivity analysis of the electrodes reveals that they integrate the signal over the entire volume comprised between the measurement electrodes. The column geometry gathers the offset of acid injection via a tube inserted at the level of the first electrode P1. At this injection point, the acid concentration is heterogeneous, resulting in a cone effect to disperse across the entire cross-section of the column. In relation to the total length to be covered, this cone effect should only be present over a thin section of a few centimetres. This cone effect could therefore pose a problem for the resolution of the P1-P4 channel compared with the P2-P4 and P3-P4 channels. However, we did not observe any significant difference in the accuracy of the modeling results between the measurement channels. On the other hand, the macroscopic advective dissolution regime certainly involves some complex channelization effects. However, as the electrical measurement is integrative over the entire volume between the electrodes, the measurement is still sensitive to dissolution, but only reflects actual behavior, which can be modeled with a 1D approximation under the imposed experimental conditions.

Therefore, the framework linking reactive transport simulation to petrophysical modeling from combined physicochemical and geoelectrical monitoring is of high interest to address multi-species reactive transport and mixing (e.g., Ghosh et al., 2018; Oliveira et al., 2020). This makes the novel approach presented in this study a relevant method for the characterization of reactive fronts across scales and systems, from the laboratory bench to groundwater contaminant plumes in regional aquifers.

In order to take complex channeling effects into account, as well as any gravitational flows, it would be interesting to model the reactive transport occurring within the column with a 3D model and a spatial resolution of a few microns. However, CrunchFlow only offers an axisymmetric model and resolution by homogenizing the concentration field over the voxel distribution. Such a 3D geometry would not suit the complexity of the problem and would require implementing a sophisticated, hybrid approach combining our reactive transport model (RTM) with a computational flow dynamics (CFD) model. Such RTM-CFD coupling frameworks have only recently been applied for 3D problems (Bao et al., 2018) and are currently under development for CrunchFlow (Li et al., 2022). While it would be interesting to explore such alternative strategies, these tasks go beyond the objectives set by this study.

4. Conclusions

This study addresses the enhancement of reactive percolation monitoring in a flow-through column through the combined use of traditional physicochemical measurements on collected water samples and geoelectrical acquisition on multiple channels along the column. The innovative aspects of the study encompass the rare level of entanglement of the geophysics and geochemistry to address the complex processes and the use of different types of acids to induce local versus extended reactive zones. Two geoelectrical methods are tested: SP and SIP. Characterization of the reaction zone spatialization, reaction rate, and porous structure changes can be achieved through the use of a workflow that couples reactive transport numerical modeling with petrophysical laws. The key findings of this study are:

- SP monitoring highlights reactive solution front propagation through the porous medium. Even a low reaction rate is detected, while the outlet pore water samples present results contrary to expectations.
- SIP imaginary conductivity enables the characterization of strong dissolution regimes. However, it is less sensitive to low reaction rates.
- The reactive transport simulations well-reproduce the outlet pore water concentrations and pH. Water electrical conductivity, porosity, and the real electrical conductivity of the sample are retrieved from petrophysical computation. Experimental data and simulation results are in accordance, whatever the reaction rate and the reactive zone extent. SP monitoring enables the characterization of concentration gradients and the extent of dissolution.

This novel study in which geophysical and geochemical methods are intrinsically intertwined paves the way to broader and more interdisciplinary studies of solute transport and reactivity in porous media. In a more general perspective, the presented methodology applies to contaminant transport.

Acknowledgment

The authors acknowledge Emmanuel Aubry for the technical support and the chemical composition analyses.

Funding sources

This work was supported by the Centre National de la Recherche Scientifique (grant number EC2CO StarTrek); and the French National Research Agency on the LabEx VOLTAIRE (grant number ANR-10-LABX-100-01).

Research Data

The experimental data, reactive transport simulation outputs, and videos of the dynamic calcite dissolution rate are available online at `https://doi.org/10.5281/zenodo.10018406`.

References

Ahmad, A., Heijnen, L., de Waal, L., Battaglia-Brunet, F., Oorthuizen, W., Pieterse, B., Bhattacharya, P., van der Wal, A., 2020. Mobility and redox transformation of arsenic during treatment of artificially recharged groundwater for drinking water production. Water Research 178, 115826. doi:`10.1016/j.watres.2020.115826`.

Archie, G.E., 1942. The electrical resistivity log as an aid in determining some reservoir characteristics. Transactions of the AIME 146, 54—-62. doi:`10.2118/942054-G`.

Atkins, P.W., de Paula, J., 2014. Molecules in motion. 8 ed.. Oxford University Press. chapter 19. pp. 747–790.

Bao, J., Zhou, T., Huang, M., Hou, Z., Perkins, W., Harding, S., Titzler, S., Hammond, G., Ren, H., Thorne, P., Suffield, S., Murray, C., Zachara, J., 2018. Modulating factors of hydrologic exchanges in a large-scale river reach: Insights from three-dimensional computational fluid dynamics simulations. Hydrological Processes 32, 3446–3463. doi:`10.1002/hyp.13266`.

Bate, B., Cao, J., Zhang, C., Hao, N., 2021. Spectral induced polarization study on enzyme induced carbonate precipitations: influences of size and content on stiffness of a fine sand. Acta Geotechnica 16, 841–857. doi:`10.1007/s11440-020-01059-8`.

Beckingham, L.E., Mitnick, E.H., Steefel, C.I., Zhang, S., Voltolini, M., Swift, A.M., Yang, L., Cole, D.R., Sheets, J.M., Ajo-Franklin, J.B., DePaolo, D.J., Mito, S., Xue, Z., 2016. Evaluation of mineral reactive surface area estimates for prediction of reactivity of a multi-mineral sediment. Geochimica et Cosmochimica Acta 188, 310–329. doi:`10.1016/j.gca.2016.05.040`.

Ben Moshe, S., Furman, A., 2022. Real-time monitoring of organic contaminant adsorption in activated carbon filters using spectral induced polarization. Water Research 212, 118103. doi:`10.1016/j.watres.2022.118103`.

Ben Moshe, S., Kessouri, P., Erlich, D., Furman, A., 2021. Geophysically based analysis of breakthrough curves and ion exchange processes in soil. Hydrology and Earth System Sciences 25, 3041–3052. doi:`10.5194/hess-25-3041-2021`.

Benson, S., Anderson, J., Bradshaw, J., Deguchi, G., Gale, J., Heidug, W., Holloway, S., Keith, D., Lloyd, P., Thomson, J., Zarlenga, F., Zhou, D., Celia, M., Lombardi, S., Oldenburg, C., Stevens, S., Borm, G., Hawkins, D., 2005. Chapter 5: Underground geological storage, in: IPCC special report on carbon dioxide capture and storage. Cambridge University Press, pp. 195–276.

Bernard, M.L., Zamora, M., Géraud, Y., Boudon, G., 2007. Transport properties of pyroclastic rocks from Montagne Pelée volcano (Martinique, Lesser Antilles). Journal of Geophysical Research: Solid Earth 112. doi:`10.1029/2006JB004385`.

Binley, A., Hubbard, S.S., Huisman, J.A., Revil, A., Robinson, D.A., Singha, K., Slater, L.D., 2015. The emergence of hydrogeophysics for improved understanding of subsurface processes over multiple scales. Water Resour. Res. 51, 3837—-3866. doi:`10.1002/2015WR017016`.

Binley, A., Slater, L., 2020. Resistivity and induced polarization: theory and applications to the near-surface earth. Cambridge University Press.

Boano, F., Harvey, J.W., Marion, A., Packman, A.I., Revelli, R., Ridolfi, L., Wörman, A., 2014. Hyporheic flow and transport processes: Mechanisms, models, and biogeochemical implications. Reviews of Geophysics 52, 603–679. doi:`10.1002/2012RG000417`.

Bufflap, S.E., Allen, H.E., 1995. Sediment pore water collection methods for trace metal analysis: A review. Water Research 29, 165–177. doi:`10.1016/0043-1354(94)E0105-F`.

Cassiani, G., Bruno, V., Villa, A., Fusi, N., Binley, A.M., 2006. A saline trace test monitored via time-lapse surface electrical resistivity tomography. Journal of Applied Geophysics 59, 244–259. doi:`10.1016/j.jappgeo.2005.10.007`.

Cherubini, A., Garcia, B., Cerepi, A., Revil, A., 2019. Influence of co_2 on the electrical conductivity and streaming potential of carbonate rocks. Journal of Geophysical Research: Solid Earth 124, 10056–10073. doi:`10.1029/2018JB017057`.

Choi, J., Hulseapple, S.M., Conklin, M.H., Harvey, J.W., 1998. Modeling CO2 degassing and ph in a stream–aquifer system. Journal of Hydrology 209, 297–310. doi:`10.1016/S0022-1694(98)00093-6`.

Chou, L., Garrels, R., Wollast, R., 1989. Comparative study of the kinetics and mechanisms of dissolution of carbonate minerals. Chemical Geology 78, 269–282. doi:`10.1016/0009-2541(89)90063-6`.

Daily, W., Ramirez, A., Labrecque, D., Nitao, J., 1992. Electrical resistivity tomography of vadose water movement. Water Resources Research 28, 1429–1442. doi:`10.1029/2009JG001129`.

Dentz, M., Le Borgne, T., Englert, A., Bijeljic, B., 2011. Mixing, spreading and reaction in heterogeneous media: A brief review. Journal of Contaminant Hydrology 120-121, 1–17. doi:`10.1016/j.jconhyd.2010.05.002`.

Eriksson, R., Merta, J., Rosenholm, J.B., 2007. The calcite/water interface: I. surface charge in indifferent electrolyte media and the influence of low-molecular-weight polyelectrolyte. Journal of Colloid and Interface Science 313, 184–193. doi:`10.1016/j.jcis.2007.04.034`.

Fernandez Visentini, A., de Anna, P., Jougnot, D., Le Borgne, T., Méheust, Y., Linde, N., 2023. Electrical signatures of diffusion-limited mixing: Insights from a milli-fluidic tracer experiment. Transport in Porous Media 146, 435–461. doi:`10.1007/s11242-021-01607-0`.

Finneran, D.W., Morse, J.W., 2009. Calcite dissolution kinetics in saline waters. Chemical Geology 268, 137–146. doi:`10.1016/j.chemgeo.2009.08.006`.

Flores Orozco, A., Ciampi, P., Katona, T., Censini, M., Petrangeli Papini, M., Deidda, G.P., Cassiani, G., 2021. Delineation of hydrocarbon contaminants with multi-frequency complex conductivity imaging. Science of The Total Environment 768, 144997. doi:`10.1016/j.scitotenv.2021.144997`.

Fredd, C.N., Miller, M.J., 2000. Validation of carbonate matrix stimulation models, in: SPE International Symposium on Formation Damage Control, Lafayette, Louisiana, OnePetro. pp. SPE–58713–MS. doi:`10.2118/58713-MS`.

Garcia-Rios, M., Cama, J., Luquot, L., Soler, J.M., 2014. Interaction between co2-rich sulfate solutions and carbonate reservoir rocks from atmospheric to supercritical co2 conditions: Experiments and modeling. Chemical Geology 383, 107–122. doi:`10.1016/j.chemgeo.2014.06.004`.

Garing, C., Luquot, L., Pezard, P.A., Gouze, P., 2014. Electrical and flow properties of highly heterogeneous carbonate rocks. AAPG Bulletin 98, 49–66. doi:`10.1306/05221312134`.

Ghosh, U., Le Borgne, T., Jougnot, D., Linde, N., Méheust, Y., 2018. Geoelectrical signatures of reactive mixing: a theoretical assessment. Geophysical Research Letters 45, 3489–3498. doi:`10.1002/2017GL076445`.

Gledhill, D.K., Morse, J.W., 2006. Calcite dissolution kinetics in na-ca-mg-cl brines. Geochimica Cosmochimica Acta 70, 5802–5813. doi:`10.1016/j.gca.2006.03.024`.

Goldscheider, N., Meiman, J., Pronk, M., Smart, C., 2008. Tracer tests in karst hydrogeology and speleology. International Journal of speleology 37, 27–40. doi:`10.5038/1827-806X.37.1.3`.

Graham, M.T., MacAllister, D., Vinogradov, J., Jackson, M.D., Butler, A.P., 2018. Self-potential as a predictor of seawater intrusion in coastal groundwater boreholes. Water Resources Research 54, 6055—-6071. doi:`10.1029/2018WR022972`.

Halisch, M., Hupfer, S., Weller, A., Dlugosch, R., Plumhoff, H.P., 2018. An experimental setup for the assessment of effects of carbonate rock dissolution on complex electrical conductivity spectra. Annual Symposium of the Society of Core Analysts (SCA) Proceedings, Trondheim, Norway , SCA2018–051.

Heberling, F., Klačić, T., Raiteri, P., Gale, J.D., Eng, P.J., Stubbs, J.E., Gil-Díaz, T., Begović, T., Lützenkirchen, J., 2021. Structure and surface complexation at the calcite(104)–water interface. Environmental Science & Technology 55, 12403–12413. doi:`10.1021/acs.est.1c03578`.

Heberling, F., Trainor, T.P., Lützenkirchen, J., Eng, P., Denecke, M.A., Bosbach, D., 2011. Structure and reactivity of the calcite–water interface. Journal of Colloid and Interface Science 354, 843–857. doi:`10.1016/j.jcis.2010.10.047`.

Hermans, T., Goderniaux, P., Jougnot, D., Fleckenstein, J.H., Brunner, P., Nguyen, F., Linde, N., Huisman, J.A., Bour, O., Lopez Alvis, J., Hoffmann, R., Palacios, A., Cooke, A.K., Pardo-Álvarez, A., Blazevic, L., Pouladi, B., Haruzi, P., Fernandez Visentini, A., Nogueira, G.E.H., Tirado-Conde, J., Looms, M.C., Kenshilikova, M., Davy, P., Le Borgne, T., 2023. Advancing measurements and representations of subsurface heterogeneity and dynamic processes: towards 4d hydrogeology. Hydrology and Earth System Sciences 27, 255–287. doi:`10.5194/hess-27-255-2023`.

Hu, K., Jougnot, D., Huang, Q., Looms, M.C., Linde, N., 2020. Advancing quantitative understanding of self-potential signatures in the critical zone through long-term monitoring. Journal of Hydrology 585, 124771. doi:`10.1016/j.jhydrol.2020.124771`.

Hubbard, S.S., Linde, N., 2011. Hydrogeophysics. 1 ed.. Elsevier. volume 2. chapter 15. pp. 401–434. doi:`10.1016/B978-0-444-53199-5.00043-9`.

Izumoto, S., Huisman, J.A., Wu, Y., Vereecken, H., 2020. Effect of solute concentration on the spectral induced polarization response of calcite precipitation. Geophysical Journal International 220, 1187—-1196. doi:`10.1093/gji/ggz515`.

Izumoto, S., Huisman, J.A., Zimmermann, E., Heyman, J., Gomez, F., Tabuteau, H., Laniel, R., Vereecken, H., Méheust, Y., Le Borgne, T., 2022. Pore-scale mechanisms for spectral induced polarization of calcite precipitation inferred from geo-electrical millifluidics. Environmental Science & Technology 56, 4998–5008. doi:`10.1021/acs.est.1c07742`.

Jougnot, D., Ghorbani, A., Revil, A., Leroy, P., Cosenza, P., 2010. Spectral induced polarization of partially saturated clay-rocks: a mechanistic approach. Geophysical Journal International 180, 210–224. doi:`10.1111/j.1365-246X.2009.04426.x`.

Jougnot, D., Jiménez-Martínez, J., Legendre, R., Le Borgne, T., Méheust, Y., Linde, N., 2018. Impact of small-scale saline tracer heterogeneity on electrical resistivity monitoring in fully and partially saturated porous media: Insights from geoelectrical milli-fluidic experiments. Advances in Water Resources 113, 295–309. doi:`10.1016/j.advwatres.2018.01.014`.

Jougnot, D., Linde, N., 2013. Self-potentials in partially saturated media: The importance of explicit modeling of electrode effects. Vadose Zone Journal 12, 1–21. doi:`10.2136/vzj2012.0169`.

Jougnot, D., Linde, N., Haarder, E.B., Looms, M.C., 2015. Monitoring of saline tracer movement with vertically distributed self-potential measurements at the HOBE agricultural test site, voulund, denmark. Journal of Hydrology 521, 314–327. doi:`10.1016/j.jhydrol.2014.11.041`.

Jougnot, D., Roubinet, D., Guarracino, L., Maineult, A., 2020. Modeling streaming potential in porous and fractured media, description and benefits of the effective excess charge density approach. Springer. chapter 4. Springer Geophysics, pp. 61–96. doi:`10.1007/978-3-030-28909-6_4`.

Jouniaux, L., Maineult, A., Naudet, V., Pessel, M., Sailhac, P., 2009. Review of self-potential methods in hydrogeophysics. Compte Rendu Geoscience 341, 928—936. doi:`10.1016/j.crte.2009.08.008`.

Kaufmann, G., Romanov, D., 2016. Structure and evolution of collapse sinkholes: Combined interpretation from physico-chemical modelling and geophysical field work. Journal of Hydrology 540, 688–698. doi:`10.1016/j.jhydrol.2016.06.050`.

Kaufmann, O., Deceuster, J., 2014. Detection and mapping of ghost-rock features in the Tournaisis area through geophysical methods – an overview. Geol. Belg. 17, 17–26.

Kemna, A., Binley, A., Cassiani, G., Niederleithinger, E., Revil, A., Slater, L.D., Williams, K.H., Orozco, A.F., Haegel, F.H., Hördt, A., Kruschwitz, S., Leroux, V., Titov, K., Zimmermann, E., 2012. An overview of the spectral induced polarization method for near-surface applications. Near Surface Geophysics 6, 453–468. doi:`10.3997/1873-0604.2012027`.

Kemna, A., Vanderborght, J., Kulessa, B., Vereecken, H., 2002. Imaging and characterisation of subsurface solute transport using electrical resistivity tomography (ert) and equivalent transport models. Journal of Hydrology 267, 125–146. doi:`10.1016/S0022-1694(02)00145-2`.

Kessouri, P., Furman, A., Huisman, J.A., Martin, T., Mellage, A., Ntarlagiannis, D., Bücker, M., Ehosioke, S., Fernandez, P., Flores-Orozco, A., Kemna, A., Nguyen, F., Pilawski, T., Saneiyan, S., Schmutz, M., Schwartz, N., Weigand, M., Wu, Y., Zhang, C., Placencia-Gomez, E., 2019. Induced polarization applied to biogeophysics: recent advances and future prospects. Near Surface Geophysics 17, 595–621. doi:`10.1002/nsg.12072`.

Knappett, P.S.K., Li, Y., Loza, I., Hernandez, H., Avilés, M., Haaf, D., Majumder, S., Huang, Y., Lynch, B., Piña, V., Wang, J., Winkel, L., Mahlknecht, J., Datta, S., Thurston, W., Terrell, D., Kirk Nordstrom, D., 2020. Rising arsenic concentrations from dewatering a geothermally influenced aquifer in central Mexico. Water Research 185, 116257. doi:`10.1016/j.watres.2020.116257`.

Leger, M., Luquot, L., Roubinet, D., 2022. Role of mineralogical, structural and hydrodynamic rock properties in conduits formation in three distinct carbonate rock types. Chemical Geology , 121008doi:`10.1016/j.chemgeo.2022.121008`.

Leroy, P., Li, S., Revil, A., Wu, Y., 2017. Modelling the evolution of complex conductivity during calcite precipitation on glass beads. Geophysical Journal International 209, 123–140. doi:`10.1093/gji/ggx001`.

Leroy, P., Revil, A., Kemna, A., Cosenza, P., Ghorbani, A., 2008. Complex conductivity of water-saturated packs of glass beads. Journal of Colloid and Interface Science 321, 103–117. doi:`10.1016/j.jcis.2007.12.031`.

Li, P., Deng, H., Molins, S., 2022. The effect of pore-scale two-phase flow on mineral reaction rates. Frontiers in Water 3, 734518. doi:`10.3389/frwa.2021.734518`.

Lichtner, P.C., 1996. Continuum formulation ofmulticomponent-multiphase reactive transport. Reviews in Mineralogy 34, 1–81.

Lowrie, W., Fichtner, A., 2020. Fundamentals of Geophysics. 3 ed., Cambridge University Press. doi:`10.1017/9781108685917`.

MacAllister, D., Jackson, M.D., Butler, A.P., Vinogradov, J., 2018. Remote detection of saline intrusion in a coastal aquifer using borehole measurements of self-potential. Water Resour. Res. 54, 1669—-1687. doi:`10.1002/2017WR021034`.

Maineult, A., Bernabé, Y., Ackerer, P., 2004. Electrical response of flow, diffusion, and advection in a laboratory sand box. Vadose Zone Journal 3, 1180–1192. doi:`10.2136/vzj2004.1180`.

Maineult, A., Bernabé, Y., Ackerer, P., 2005. Detection of advected concentration and ph fronts from self-potential measurements. Journal of Geophysical Research 110, B11205. doi:`10.1029/2005JB003824`.

Maineult, A., Jouniaux, L., Bernabé, Y., 2006. Influence of the mineralogical composition on the self-potential response to advection of kcl concentration fronts through sand. Geophysical Research Letter 33. doi:`10.1029/2006GL028048`.

Mao, D., Revil, A., Hort, R.D., Munakata-Marr, J., Atekwana, E.A., Kulessa, B., 2015. Resistivity and self-potential tomography applied to groundwater remediation and contaminant plumes: Sandbox and field experiments. Journal of Hydrology 530, 1–14. doi:`10.1016/j.jhydrol.2015.09.031`.

Mito, S., Xue, Z., T., S., 2013. Effect of formation water composition on predicting co2 behavior: A case study at the nagaoka post-injection monitoring site. Applied Geochemistry 30, 33–40. doi:`10.1016/j.apgeochem.2012.08.020`.

Molins, S., Trebotich, D., Yang, L., Ajo-Franklin, J.B., Ligocki, T.J., Shen, C., Steefel, C.I., 2014. Pore-scale controls on calcite dissolution rates from flow-through laboratory and numerical experiments. Environmental Science & Technology 48, 7453–7460. doi:`10.1021/es5013438`.

Morse, J.W., Arvidson, R.S., Lüttge, A., 2007. Calcium carbonate formation and dissolution. Chemical Reviews 107, 342–281. doi:`10.1021/cr050358j`.

Murtaza, Y., Leinov, G.E., Jackson, M.D., 2011. Self-potential anomalies induced by water injection into hydrocarbon reservoirs. Geophysics 76, F283–F292. doi:`10.1190/1.3596010`.

Niu, Q., Zhang, C., 2019. Permeability prediction in rocks experiencing mineral precipitation and dissolution: a numerical study. Water Resources Research 55, 3107–3121. doi:`10.1029/2018WR024174`.

Noiriel, C., Gouze, P., Bernard, D., 2004. Investigation of porosity and permeability effects from microstructure changes during limestone dissolution. Geophysical Research Letters 31, L24603. doi:`10.1029/2004GL021572`.

Oliveira, T.D.S., Blunt, M.J., Bijeljic, B., 2020. Multispecies reactive transport in a microporous rock: Impact of flow heterogeneity and reversibility of reaction. Water Resources Research 56, e2020WR027317. doi:`10.1029/2020WR027317`.

Palacios, A., Ledo, J.J., Linde, N., Luquot, L., Bellmunt, F., Folch, A., Marcuello, A., Queralt, P., Pezard, P.A., Martinez, L., del Val, L., Bosch, D., Carrera, J., 2020. Time-lapse cross-hole electrical resistivity tomography (chert) for monitoring seawater intrusion dynamics in a mediterranean aquifer. Hydrology and Earth System Sciences 24, 2121–2139. doi:`10.5194/hess-24-2121-2020`.

Palandri, J.L., Kharaka, Y.K., 2004. A compilation of rate parameters of water–mineral interaction kinetics for application to geochemical modeling. Technical Report. Geological Survey Menlo Park CA.

Petiau, G., Dupis, A., 1980. Noise, temperature coefficient, and long time stability of electrodes for telluric observations. Geophysical Prospecting 28, 792–804. doi:`10.1111/j.1365-2478.1980.tb01261.x`.

Plummer, L.N., Busenberg, E., 1982. The solubilities of calcite, aragonite and vaterite in co2-h2o solutions between 0 and 90°C, and an evaluation of the aqueous model for the system caco3-co2-h2o. Geochimica et Cosmochimica Acta 46, 1011—-1040. doi:10.1016/0016âĂŘ7037(82)90056âĂŘ4.

Plummer, L.N., Wigley, T.M.L., Parkhurst, D.L., 1978. The kinetics of calcite dissolution in co 2 -water systems at 5 degrees to 60 degrees c and 0.0 to 1.0 atm co2. American Journal of Science 278, 179—-216. doi:10.2475/ajs.278.2.179.

Pokrovsky, O., Golubev, S., Schott, J., 2005. Dissolution kinetics of calcite, dolomite and magnesite at 25^{o}c and 0 to 50 atm pco2. Chemical Geology 217, 239—-255. doi:10.1016/j.chemgeo.2004.12.012.

Quincke, G., 1859. Ueber eine neue art elektrischer ströme. Annalen der Physik 183, 1–47. doi:10.1002/andp.18591830502.

Rattray, M., Mitsuda, E., 1974. Theoretical analysis of conditions in a salt wedge. Estuarine and Coastal Marine Science 2, 375–394. doi:10.1016/0302-3524(74)90006-1.

Rembert, F., 2021. Development of geo-electrical methods to characterize dissolution and precipitation processes in a carbonate context. phdthesis. Sorbonne Université.

Rembert, F., Jougnot, D., Guarracino, L., 2020. A fractal model for the electrical conductivity of water-saturated porous media during mineral precipitation-dissolution processes. Advances in Water Resources 145, 103742. doi:`10.1016/j.advwatres.2020.103742`.

Rembert, F., Jougnot, D., Luquot, L., Guérin, R., 2022. Interpreting self-potential signal during reactive transport: application to calcite dissolution and precipitation. Water 14, 1632. doi:`10.3390/w14101632`.

Rembert, F., Léger, M., Jougnot, D., Luquot, L., 2023a. Geoelectrical and hydro-chemical monitoring of karst formation at the laboratory scale. Hydrology and Earth System Sciences 27, 417–430. doi:`10.5194/hess-27-417-2023`.

Rembert, F., Stolz, A., Soulaine, C., Roman, S., 2023b. A microfluidic chip equipped for geoelectrical monitoring of the critical zone processes. Lab on a Chip 23, 3433–3442. doi:`10.1039/D3LC00377A`.

Revil, A., 1999. Ionic diffusivity, electrical conductivity, membrane and thermoelectric potentials in colloids and granular porous media: A unified model. Journal of Colloid and Interface Science 212, 503–522. doi:`10.1006/jcis.1998.6077`.

Revil, A., Jardani, A., 2013. The Self-Potential Method: Theory and Applications in Environmental Geosciences. Cambridge University Press. doi:`10.1017/cbo9781139094252`.

Revil, A., Karaoulis, M., Johnson, T., Kemna, A., 2012a. Some low-frequency electrical methods for subsurface characterization and monitoring in hydrogeology. Hydrogeology Journal 20, 617–658. doi:`10.1007/s10040-011-0819-x`.

Revil, A., Koch, K., Holliger, K., 2012b. Is it the grain size or the characteristic pore size that controls the induced polarization relaxation time of clean sands and sandstones? Water Resources Research 48, W05602. doi:`10.1029/2011WR011561`.

Revil, A., Leroy, P., 2004. Constitutive equations for ionic transport in porous shales. Journal of Geophysical Research 109, B03208. doi:`10.1029/2003JB002755`.

Revil, A., Linde, N., 2006. Chemico-electromechanical coupling in microporous media. Journal of Colloid and Interface Science 302, 682–694. doi:`10.1016/j.jcis.2006.06.051`.

Rubin, Y., Hubbard, S.S. (Eds.), 2006. Hydrogeophysics. volume 50. Springer Science & Business Media.

Saneiyan, S., Ntarlagiannis, D., Ohan, J., Lee, J., Colwell, F., Burns, S., 2019. Induced polarization as a monitoring tool for in-situ microbial induced carbonate precipitation (micp) processes. Ecological Engineering 127, 36–47. doi:`10.1016/j.ecoleng.2018.11.010`.

Singha, K., Day-Lewis, F.D., Johnson, T., Slater, L., 2015. Advances in interpretation of subsurface processes with time-lapse electrical imaging. Hydrological Processes 29, 1549–1576. doi:`10.1002/hyp.10280`.

Singha, K., Gorelick, S.M., 2005. Saline tracer visualized with three-dimensional electrical resistivity tomography: Field-scale spatial moment analysis. Water Resources Research 41, W05023. doi:`10.1029/2004WR003460`.

Singha, K., Li, L., Day-Lewis, F.D., Regberg, A.B., 2011. Quantifying solute transport processes: Are chemically “conservative” tracers electrically conservative? Geophysics 76, F53–F63. doi:`10.1190/1.3511356`.

Sjöberg, E.L., Rickard, D., 1984. Calcite dissolution kinetics: surface speciation and the origin of the variable ph dependence. Chemical Geology 42, 119–136. doi:`10.1016/0009-2541(84)90009-3`.

Soldi, M., Guarracino, L., Jougnot, D., 2020. An effective excess charge model to describe hysteresis effects on streaming potential. Journal of Hydrology 588, 124949. doi:`10.1016/j.jhydrol.2020.124949`.

Steefel, C.I., 2009. CrunchFlow. Software for modeling multicomponent reactive flow and transport. User’s Manual.

Steefel, C.I., Appelo, C.A.J., Arora, B., Jacques, D., Kalbacher, T., Kolditz, O., Lagneau, V., Lichtner, P.C., Mayer, K.U., Meeussen, J.C.L., Molins, S., Moulton, D., Shao, H., Šimůnek, J., Spycher, N., Yabusaki, S.B., Yeh, G.T., 2015. Reactive transport codes for subsurface environmental simulation. Computational Geosciences 19, 445–478.

Steefel, C.I., Lichtner, P.C., 1998. Multicomponent reactive transport in discrete fractures: I. controls on reaction front geometry. Journal of Hydrology 209, 186–199. doi:`10.1016/S0022âĂŘ1694(98)00146âĂŘ2`.

Stevenson, D., 1997. Flow and filtration through granular media—the effect of grain and particle size dispersion. Water Research 31, 310–322. doi:`10.1016/S0043-1354(96)00271-0`.

Sun, Z., Mehmani, A., Torres-Verdín, C., 2021. Pore-scale investigation of the electrical resistivity of saturated porous media: flow patterns and porosity efficiency. Journal of Geophysical Research: Solid Earth 126, e2021JB022608. doi:`10.1029/2021JB022608`.

Werner, A.D., Bakker, M., Post, V.E.A., Vandenbohede, A., Lu, C., Ataie-Ashtiani, B., Simmons, C.T., Barry, D.A., 2013. Seawater intrusion processes, investigation and management: Recent advances and future challenges. Advances in Water Resources 51, 3–26. doi:`10.1016/j.advwatres.2012.03.004`.

Wu, Y., Hubbard, S., Williams, K.H., Ajo-Franklin, J., 2010. On the complex conductivity signatures of calcite precipitation. Journal of Geophysical Research 115, G00G04. doi:`10.1029/2009JG001129`.

Zhang, C., Slater, L., Redden, G., Fujita, Y., Johnson, T., Fox, D., 2012. Spectral induced polarization signatures of hydroxide adsorption and mineral precipitation in porous media. Environmental Science & Technology 46, 4357–4364. doi:`10.1021/es204404e`.

Zimmermann, E., Kemna, A., Berwix, J., Glaas, W., Münch, H.M., Huisman, J.A., 2008. A high-accuracy impedance spectrometer for measuring sediments with low polarizability. Measurement Science and Technology 19, 105603. doi:`10.1088/0957-0233/19/10/105603`.